An intercomparison between AMSR-E snow-depth and satellite C- and Ku-band radar backscatter data for Antarctic sea ice

Stefan KERN,[1] Burcu OZSOY-CICEK,[2] Sascha WILLMES,[3] Marcel NICOLAUS,[4] Christian HAAS,[5] Stephen ACKLEY[2]

[1]*Center for Marine and Atmospheric Science, Institute of Oceanography, University of Hamburg, Bundesstrasse 53, D-20146 Hamburg, Germany*
E-mail: stefan.kern@zmaw.de
[2]*Laboratory for Remote Sensing and Geoinformatics, Department of Geological Sciences, University of San Antonio, San Antonio, TX 78249, USA*
[3]*Department of Environmental Meteorology, University of Trier, Behringstrasse 21, D-54286 Trier, Germany*
[4]*Alfred Wegener Institute for Polar and Marine Research, PO Box 120161, D-27515 Bremerhaven, Germany*
[5]*Department of Earth and Atmospheric Sciences, University of Alberta, Edmonton, Alberta T6G 2E3, Canada*

ABSTRACT. Advanced Microwave Scanning Radiometer (AMSR-E) snow-depth data for Antarctic sea ice are compared with ship-based visual observations of snow depth, ice type and ridged-ice fraction, and with satellite C-band and Ku-band radar backscatter observations for two ship cruises into the Weddell Sea (ISPOL 2004–05, WWOS 2006) and one cruise into the Bellingshausen Sea (SIMBA 2007) during late winter/spring. Most (>75%) AMSR-E and ship-based snow-depth observations agree within 0.2 m during WWOS and SIMBA. Remaining observations indicate substantial underestimations of snow depths by AMSR-E data. These underestimations tend to increase with the ridged-ice fraction for WWOS and SIMBA. In areas with large snow depths, a combination of relatively stable low C-band radar backscatter and variable Ku-band radar backscatter is associated with undeformed first-year ice and may indicate snow metamorphism at this time of year during SIMBA. In areas with small snow depths, a combination of relatively stable low Ku-band radar backscatter, high C-band radar backscatter and low C-band radar backscatter standard deviations is associated with rough first-year ice during SIMBA. This information can help to better understand causes of the observed AMSR-E snow-depth bias during late-winter/spring conditions with decreasing average snow depth and to delineate areas where this bias occurs.

1. INTRODUCTION

Snow on sea ice is a crucial component of the polar cryosphere. It insulates sea ice against atmospheric processes and influences the net shortwave radiation flux at and within the sea ice with a number of implications for sea-ice physics (ice growth and melt) as well as biota (availability of shortwave radiation) (e.g. Massom and others, 2001). Snow-to-ice conversion due to flooding of the sea ice with subsequent refreezing is hypothesized to play a considerable role for the Antarctic sea-ice mass balance (e.g. Maksym and Markus, 2008). Accurate knowledge of the snow depth on sea ice is essential to the accurate modelling of ocean–ice–atmosphere heat and energy fluxes, and the derivation of the ice thickness using satellite altimetry (Fichefet and Morales Maqueda, 1999; Kwok and others, 2006; Wingham and others, 2006).

However, while satellite microwave radiometry permits circum-Antarctic snow depth estimates, the accuracy of this snow depth product is still under debate. A case study, based on observations carried out during the Sea Ice Mass Balance in the Antarctic (SIMBA) ice drift station in the Bellingshausen Sea in 2007 (Ozsoy-Cicek and others, in press), confirmed findings of other expeditions (e.g. in East Antarctica (Worby and others, 2008)): an underestimation of Advanced Microwave Scanning Radiometer–Earth Observing System (AMSR-E) snow depths over rough sea ice by a factor of 2.3.

In this study, we build on the results of the case study of Ozsoy-Cicek and others (in press). AMSR-E snow depth measurements are compared with more visual ship-based observations carried out according to the Antarctic Sea Ice Processes and Climate (ASPeCt) protocol (henceforth called ASPeCt snow depth) during SIMBA and two other cruises which took place in the Weddell Sea, i.e. Ice Station POLarstern (ISPOL 2004–05) and Winter Weddell Outflow Study (WWOS 2006). The aim is to identify regions and ice types for which ASPeCt and AMSR-E snow depth values agree or disagree.

In order to do this, we compare coincident satellite C-band (Envisat Advanced Synthetic Aperture Radar (ASAR)) and Ku-band (SeaWinds QuikSCAT) radar backscatter (henceforth abbreviated with σ^0_C and σ^0_{Ku}) data with ASPeCt and AMSR-E snow depth data along the cruise tracks and also on the scale of the acquired ASAR images in order to seek possible relationships between changes in the mean snow depth distribution and observed dual-frequency σ^0 values. Values of σ^0_C are sensitive to changing snow microwave dielectric properties due to snow metamorphism and summer melt as shown for perennial sea ice by Haas (2001), for example. Radar backscatter data are sensitive to the presence of meltwater in the snow at both C- and Ku-band. The onset of snow metamorphism, that is an increase in snow grain size and a change in the vertical layering of the snowpack due to alternating melt–freeze cycles, is a precursor to summer snowmelt. It is, however, more likely to be detected at Ku- than at C-band (Willmes and others, 2010), because the initial changes in the snow microwave dielectric properties due to a non-permanent, relatively low snow wetness, and the still relatively small snow grains (associated with the onset of snow metamorphism) have smaller impacts on σ^0_C than on σ^0_{Ku}.

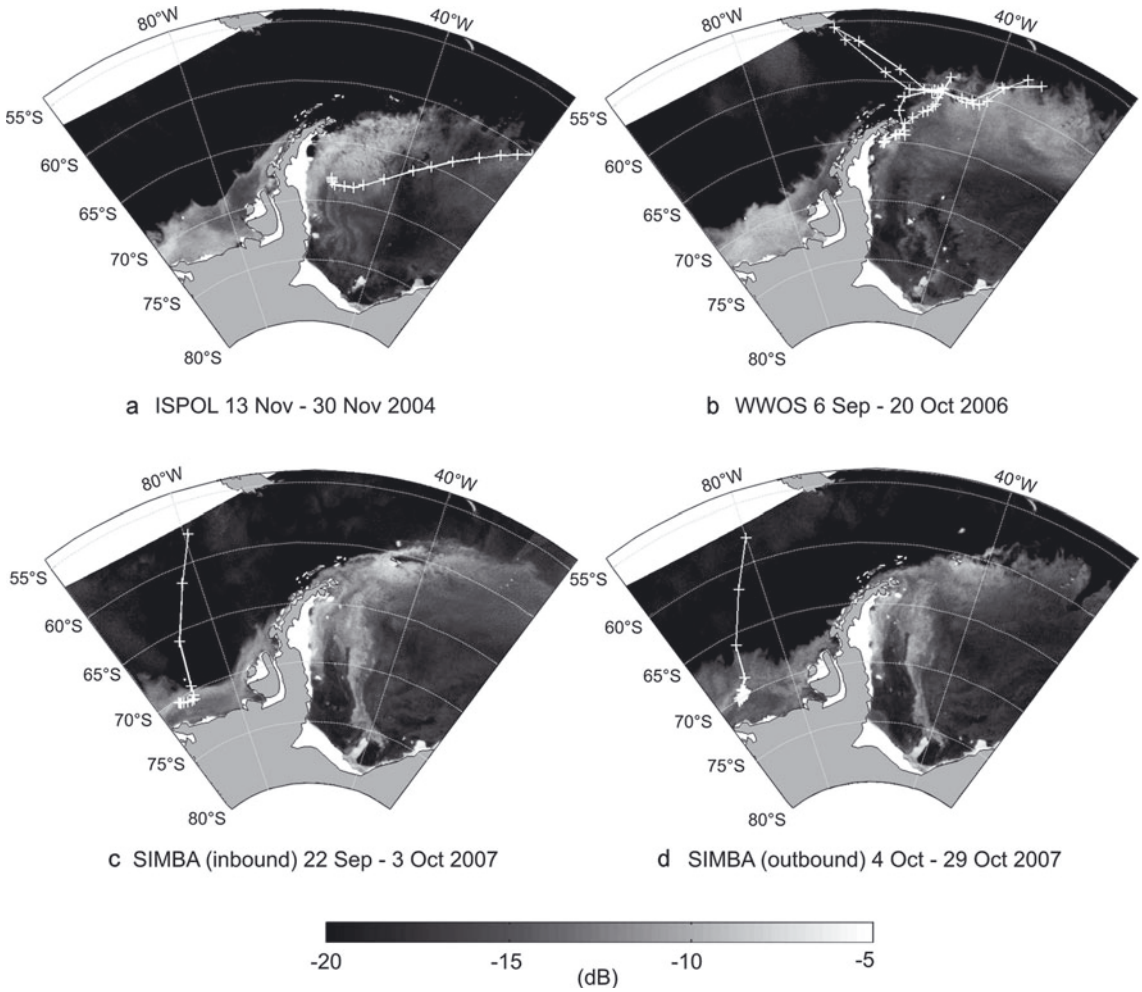

Fig. 1. Mean σ^0_{KuHH} derived from resolution-enhanced QuikSCAT data for ISPOL (a), WWOS (b) and SIMBA in- and outbound legs (c, d). The averaging period is given below each image. Connected white plus signs denote the ship's tracks in daily intervals. Note that for 27–30 November 2004 (a), 27 September–3 October 2007 (c) and 4–24 October 2007 (d), the ship was drifting with the sea ice.

We investigate satellite data coincident with cruises that took place in the late winter/spring (September–November). Therefore we expect to see the influence of snow metamorphism on the coincident satellite radar backscatter data. Together with the results of the comparison between ASPeCt and AMSR-E snow depth data along the ship tracks, we hope to gain more information about the spatio-temporal distribution of potential snow-depth underestimation by AMSR-E from the satellite data.

2. DATA

In the present paper, a comparison between ship-based observations of snow and sea-ice properties and satellite-based snow and sea-ice radar backscatter observations is carried out. Our regions of interest, within the Weddell Sea and the Bellingshausen Sea, are shown in Figure 1 where cruise tracks (see section 2.1) are superposed on maps of the average σ^0_{Ku} obtained from QuikSCAT data.

2.1. Ship-based sea-ice and snow observations

Ship-based visual observations were carried out hourly from the ship's bridge within an observation radius of ~1 km according to the ASPeCt protocol (Worby and others, 1999; http://www.aspect.aq) as the ship moved through the sea ice. Ice type observations included concentration, level ice thickness, floe size, topography (i.e. ridge sail height and fractional coverage of ridges), snow cover type and snow depth. Snow depths are typically given to the nearest 0.1 m; ridge sail height and fraction are given to the nearest 0.5 m interval and 10%, respectively. Snow depth estimation during each observation was done by observing overturning ice blocks over the side of the ship and occasionally measuring the depth of snow with a suspended gauge stick as a visual reference for scale.

The ISPOL cruise visited the western Weddell Sea from November 2004 to January 2005 (Hellmer and others, 2008). Comprehensive measurements of snow properties, particularly snow thickness, were performed during transects to and from a drift station at approximately 67° S, 56° W (Fig. 1a). During WWOS in September and October 2006, similar measurements were performed in the outflowing branch of old ice of the northwestern Weddell Sea (Haas and others, 2009) (Fig. 1b). Snow and ice properties along transects on the sea ice during both these cruises are discussed in conjunction with σ^0_{Ku} derived from QuikSCAT data in Willmes and others (in press). Here we consider ASPeCt observations carried out during the entire WWOS cruise (total 444 individual observations) and the inbound leg of the ISPOL cruise (total 205 individual observations). The SIMBA cruise visited the Bellingshausen Sea at ~90° W. The aim was to investigate the change in sea-ice and snow properties in

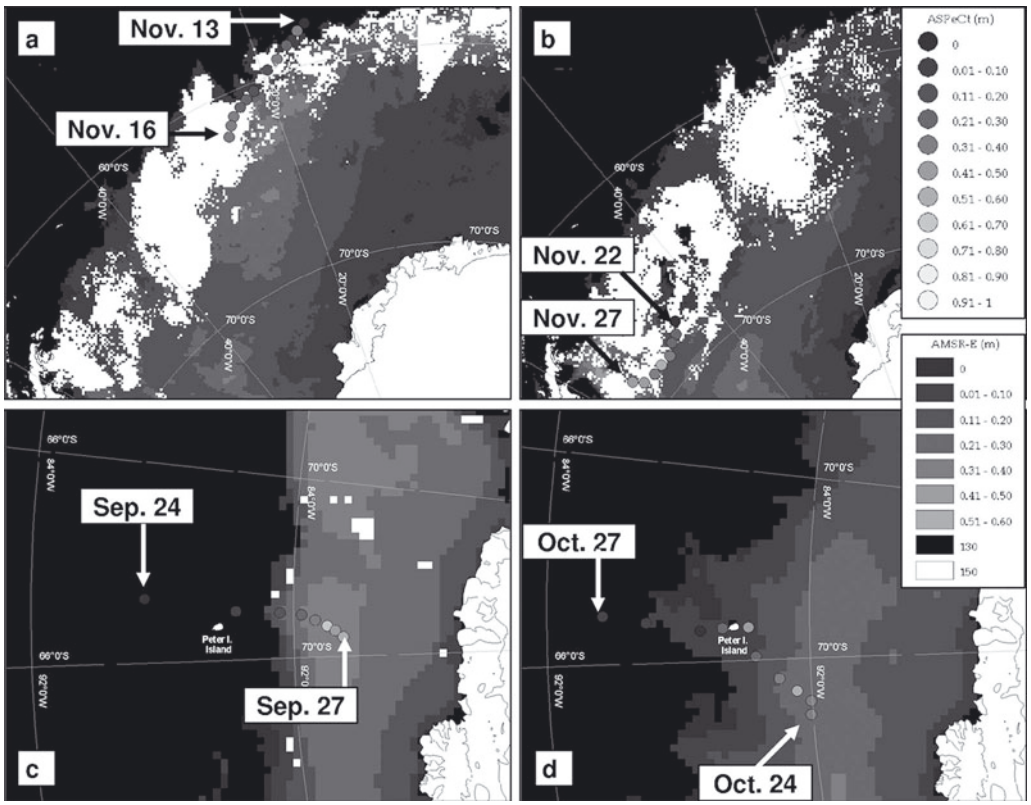

Fig. 2. Maps of the AMSR-E snow depth superimposed with 6 hour averages of the ASPeCt snow depth at the respective mean ship positions for ISPOL (a, b), and SIMBA (c, d). White gridcells mark values flagged as 150. Background AMSR-E snow depth maps are from 16 and 27 November 2004 (a, b) and 27 September and 27 October 2007 (c, d). The legends on the right-hand side are valid for all four images shown.

the late-winter/spring transition period (September–October) during an ice drift station (Lewis and others, in press). ASPeCt observations carried out during both the inbound leg (total 52 individual observations; Fig. 1c) and the outbound leg (total 59 individual observations; Fig. 1d) of the SIMBA cruise are considered in this paper.

2.2. AMSR-E snow depth data

In this study, we use sea-ice concentration and the snow depth data from 'AMSR-E/Aqua Daily L3 12.5 km Tb, Sea Ice Conc., & Snow Depth Polar Grids, Version 12' provided by the US National Snow and Ice Data Center (NSIDC). These products are based on analysis of the 18.7 and 36.5 GHz channels which have a footprint size of 16 km x 27 km and 8 km × 14 km, respectively. The sea-ice concentration and snow depth product is available on polar stereographic projection centered at 70° S with 12.5 km grid resolution (D.J. Cavalieri and others, http://nsidc.org/data/docs/daac/ae_si12_12km_tb_sea_ice_and_snow.gd.html). The snow depth is retrieved using an empirical formula based on the normalized spectral gradient ratio (GR) between vertical brightness temperatures (TBV) measured at 37 and 19 GHz (Markus and Cavalieri, 1998; Comiso and others, 2003). Before GR is calculated, the ice concentration is used to obtain the pure ice brightness temperature (TB) because the open-water influence must be eliminated to obtain a reasonable estimate of the snow depth using the GR. The GR is close to zero for bare first-year ice and becomes negative with increasing snow depth. This is because of the microwave radiation emitted by the sea ice which is scattered by snow more at 37 than at 19 GHz. This results in relatively larger TBV values at 19 than at 37 GHz. The maximum snow depth that can be retrieved is 0.5 m. For details and limitations of this algorithm, see Markus and Cavalieri (1998), Markus and others, (2006a,b) and Stroeve and others (2006). The AMSR-E snow depth product used is a daily product. Data are provided as a 5 day running average including the actual day and the four preceding days to mitigate uncertainties caused by the influence of snow grain size and density variations. Examples of the AMSR-E snow depth distribution are given in Figure 2.

The AMSR-E snow depth product includes a number of flags. Over open water and ice concentrations below 20%, snow depths are flagged as 130. One other flag, which is relevant for this study, has the value 150. This flag is used when (1) the microwave properties of the underlying sea ice are similar to multi-year (MY) ice, which generally causes negative GR and thus an overestimation of the snow depth, and (2) melt–refreeze-cycles cause periods of dry very coarse-grained snow and wet snow, which causes a high temporal variation of the GR and thus a high and unlikely day-to-day variation in the snow depth. In both cases, no snow depth value is provided and the respective gridcell is flagged as 150. For the late-winter/spring cruises (SIMBA and WWOS, September/October), areas flagged as 150 are relatively sparse. These areas are, however, a persistent feature during ISPOL which took place in November. At this time of year, snowmelt has commenced and might have caused high diurnal as well as day-to-day variations in the snow properties (Haas, 2001) and the TB values (e.g. Willmes and others, 2006), and hence in the AMSR-E snow depth. Between one-third and half of the Weddell Sea area between 0° and 60° W is flagged as 150 during ISPOL (Fig. 2).

2.3. Radar backscatter observations

2.3.1. SeaWinds QuikSCAT Scatterometer

The SeaWinds sensor on the polar-orbiting QuikSCAT satellite is a conically scanning pencil-beam scatterometer operating in Ku-band at a frequency of 13.4 GHz (wavelength 2.2 cm). The instrument makes dual polarization surface backscatter measurements in a continuous 1800 km wide band centered on the spacecraft's nadir subtrack. The antenna scans two footprint paths at incidence angles of 46° (HH-polarized) and 54° (VV-polarized). For a comparison with AMSR-E snow depth data, σ^0_{Ku} reprocessed with the Scatterometer Image Reconstruction (SIR) algorithm were used (Early and Long, 2001). These data were acquired from the Brigham Young University (BYU) Center for Remote Sensing. The SIR algorithm combines QuikSCAT Level 1B slice radar backscatter measurements ($6 \times 25\,km^2$) from multiple azimuth angles and multiple orbit passes collected over the imaging period. The resulting images provide an enhanced effective resolution of ~5 km and represent a nonlinear weighted average of the single backscatter measurements. An implicit assumption is that the surface characteristics remain constant over the imaging period. We extracted σ^0_{Ku} at horizontal and vertical polarization, σ^0_{KuHH} and σ^0_{KuVV}, as well as standard deviations, which denote the temporal variation and azimuth modulation within each pixel. For a comparison with AMSR-E and Envisat ASAR, QuikSCAT data were resampled to a common 12.5 km polar stereographic grid centred at 70° S. By using SIR data, we made a better assessment of the variability within each gridcell through their higher effective resolution. Figure 1 shows the mean σ^0_{KuHH} for ISPOL, WWOS and SIMBA.

2.3.2. Envisat Advanced Synthetic Aperture Radar (ASAR)

For this study, we use HH-polarization Wide Swath Mode (WSM) images from the Envisat C-band (frequency 5.3 GHz, wavelength 5.6 cm) ASAR (Attema and others, 1998). These are provided with a pixel size of 75 m × 75 m and a swath width of ~400 km. Geolocation accuracy of these images is of the order of 100–200 m (personal communication from L.T. Pedersen, 2010) but can be shifted by up to 1 km. However, since we upscale the ASAR images to 12.5 km grid resolution (see below), such a shift would be of minor relevance. All ASAR images used (6 for WWOS, 19 for ISPOL and 56 for SIMBA) were geolocated, calibrated (e.g. Huang and Siegert, 2004) and projected onto a polar stereographic grid centred at 70° S with 125 m grid resolution. For comparison with all other datasets (ASPeCt observations, QuikSCAT σ^0_{Ku}, AMSR-E snow depth), the projected ASAR data were upscaled to 12.5 km grid resolution by calculating the mean HH-polarized σ^0_C (σ^0_{CHH}) for each co-located 12.5 km AMSR-E snow depth (and QuikSCAT σ^0_{Ku}) gridcell; the σ^0_{CHH} standard deviation was computed as well for these gridcells.

3. METHODS

We compare ASPeCt observations of snow depth, ice type, and fraction of ridged ice with coincident AMSR-E snow depths. For each individual ASPeCt observation, we first computed a mean snow depth value which is the ice-type fraction weighted mean of the snow depths on the ice types reported (up to three). We compared the corresponding value of this mean snow depth of each individual ASPeCt observation (total numbers of observations for each cruise are given in section 2 above) and each co-located AMSR-E (12.5 km × 12.5 km) gridcell. In order to find this gridcell, we took the position of the ship at the time of an ASPeCt observation and found the equivalent AMSR-E gridcell on that day within a minimum distance of the ship position.

In order to display the location of ASPeCt snow depth observations in comparison with coincident AMSR-E snow depth distribution, we computed 6 hourly averages of the mean (see above) ASPeCt snow depth. These averages comprise observations for time intervals 0–5 UTC, 6–11 UTC, etc. These averages are shown in Figure 2 superposed at the mean ship's position onto the AMSR-E snow depth distribution (5 day average) for the periods 12–16 November 2004 (Fig. 2a), 23–27 November 2004 (Fig. 2b), 23–27 September 2007 (Fig. 2c) and 23–27 October 2007 (Fig. 2d), for ISPOL ASPeCt observation periods 13–16 November 2004 and 23–27 November 2004 (Fig. 2a and b) and for SIMBA ASPeCt observation periods 24–27 September 2007 (inbound leg) and 24–27 October 2007 (outbound leg).

For the purpose of relating ASPeCt and AMSR-E snow depths to the observed ice type and fraction of ridged ice, we estimated the dominant ice type by visual inspection of the ASPeCt ice type observations, and we computed an ice type fraction weighted mean of the ASPeCt observations of the fraction of ridged ice. These data are combined in Figure 3, and Figure 4 shows ASPeCt and AMSR-E snow depth data together with the fraction of ridged ice.

We also compare snow depth data with coincident σ^0 values obtained at C- and Ku-band. This is done by (1) using only ASPeCt and coincident AMSR-E snow-depth data along the cruise tracks of SIMBA and ISPOL, and (2) using AMSR-E snow depths that were co-located with the used Envisat ASAR images acquired during SIMBA.

For (1), we compared the mean snow depth of each individual ASPeCt observation (see above) with the coincident AMSR-E snow depth (at 12.5 km × 12.5 km grid resolution) and the coincident σ^0_{CHH}, σ^0_{KuHH} and σ^0_{KuVV} values obtained from ASAR and QuikSCAT imagery, also at 12.5 km × 12.5 km grid resolution (see section 2). Only ASAR images within an acquisition time within 1.5 hours of an ASPeCt observation were considered, i.e. 5, 0 and 3 ASAR images for SIMBA, WWOS and ISPOL, respectively. The appropriate 12.5 km × 12.5 km gridcell was found as described above.

For (2), we used all daily AMSR-E and QuikSCAT gridcells which coincide with an ASAR image acquired during SIMBA and where the ice concentration according to the AMSR-E product exceeds 60%. ASAR images were put into five groups according to their acquisition time: 12:50 UTC, 6:50 UTC (named PETERIA_ASC), 13:30 UTC (named PETERIA_DES), 6:30 UTC and 13:10 UTC. Only ASAR images acquired within 15 min of these times were used (10, 9, 10, 8 and 6 images per group, respectively). For each group, we generated a mask containing only gridcells where at least two-thirds of the images, which belong to one group, overlap with each other. We used this mask for every group to limit the comparison between AMSR-E snow depth, σ^0_{CHH}, σ^0_{KuHH} and σ^0_{KuVV}. For each set of AMSR-E snow-depth–σ^0_{Ku}–σ^0_C maps, we looked at: (1) histograms of AMSR-E snow depth; (2) histograms of mean σ^0_{CHH}, σ^0_{KuHH} and σ^0_{KuVV} (note that this is always an average for 12.5 km grid resolution gridcells) as well as their standard deviations,

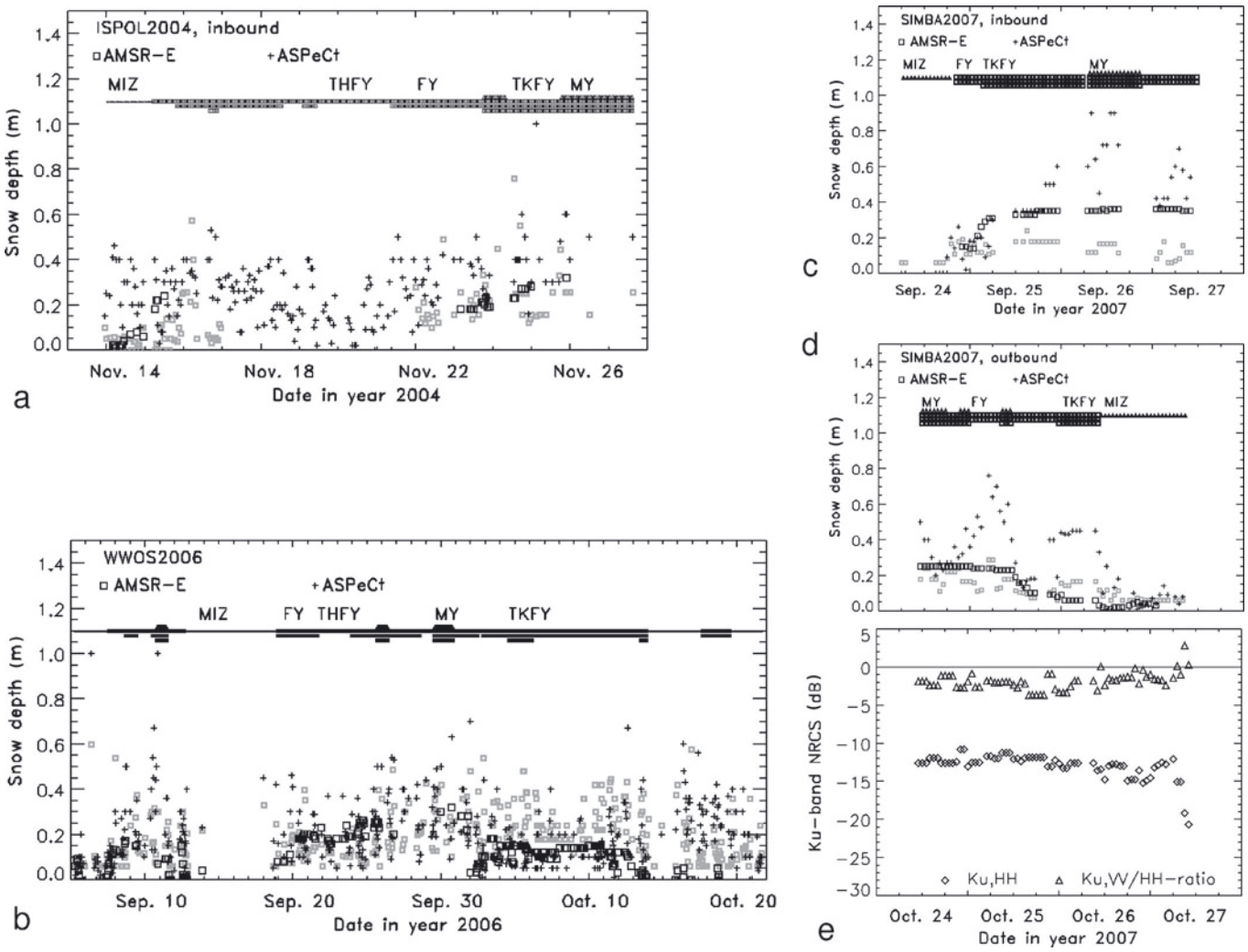

Fig. 3. (a–d) Comparison between ASPeCt snow depth and co-located AMSR-E snow depth for (a) ISPOL, (b) WWOS, (c) SIMBA inbound and (d) SIMBA outbound cruises. (e) Ku-band HH-polarization radar backscatter values (diamonds) and the VV-/HH-polarization ratio (triangles) coincident and co-located with (d). Gridcells with snow depth values flagged as 130 or 150 are omitted. AMSR-E snow depth data of 17–21 November for ISPOL are missing. Symbols given at ~1.1 m snow depth denote the dominant ice type according to the ASPeCt observations. Different symbols and different vertical extent of these symbols denote different ice types: marginal ice zone (MIZ), thin first-year ice (THFY), medium thick first-year ice (FY), thick first-year ice (TKFY) and multi-year ice (MY). Grey squares denote the fraction of ridged ice according to the ASPeCt observations; this fraction is scaled as the snow depth: 0.2 (0.4) means 20% (40%) of the observed sea ice was ridged. Data gaps in (a), (c) and (d) are due to missing observations or satellite data; the longer gap in (b) is due to the ship operating outside the ice cover.

and of the Ku-band VV/HH-polarization ratio; and (3) scatter plots of σ^0_{CHH} vs its standard deviation and of σ^0_{KuHH} vs σ^0_{CHH} scaled with the coincident AMSR-E snow depth.

4. RESULTS AND DISCUSSION

4.1. ASPeCt snow depth versus AMSR-E snow depth

In Figure 2, we compare averages of the ASPeCt snow depth observations (see section 3) with the AMSR-E snow depth. Large areas are flagged with a value of 150 in Figure 2a and b, thereby indicating that no snow-depth value can be retrieved due to melting conditions, and/or melt–refreeze conditions, and/or presence of MY ice. It is difficult to identify from Figure 2a and b, which show ISPOL data, whether ASPeCt and AMSR-E snow depths agree with each other. These images clearly highlight the problem of data availability in a region such as the northwestern Weddell Sea during November. This region is subject to frequent overpasses of low-pressure systems which may cause frequently changing snow surface properties and bring into play the limitations for the snow-depth retrieval already described. Figure 2c and d, which show SIMBA data, highlight the problem of a strongly varying ice-edge location: ASPeCt snow depth observations occur in regions where AMSR-E snow depth is flagged open water or <20% ice concentration. Apart from this, ASPeCt and AMSR-E snow depths tend not to agree as well as they do in the Weddell Sea (Fig. 2a and b). We do not show similar maps for the WWOS cruise because it was of much longer duration (5 September–20 October 2006) than the other cruises.

Figure 3a–d show mean individual ASPeCt snow depths along all used cruise tracks (see Fig. 1 and section 3) in comparison to coincident AMSR-E snow depths. Together with the snow depth, we show the dominant ice type and the fraction of ridged ice, in order to check whether (1) AMSR-E snow depths are flagged as 150 in case MY ice was observed, and (2) a difference/bias between AMSR-E and ASPeCt snow depths increases with the observed fraction of ridged ice.

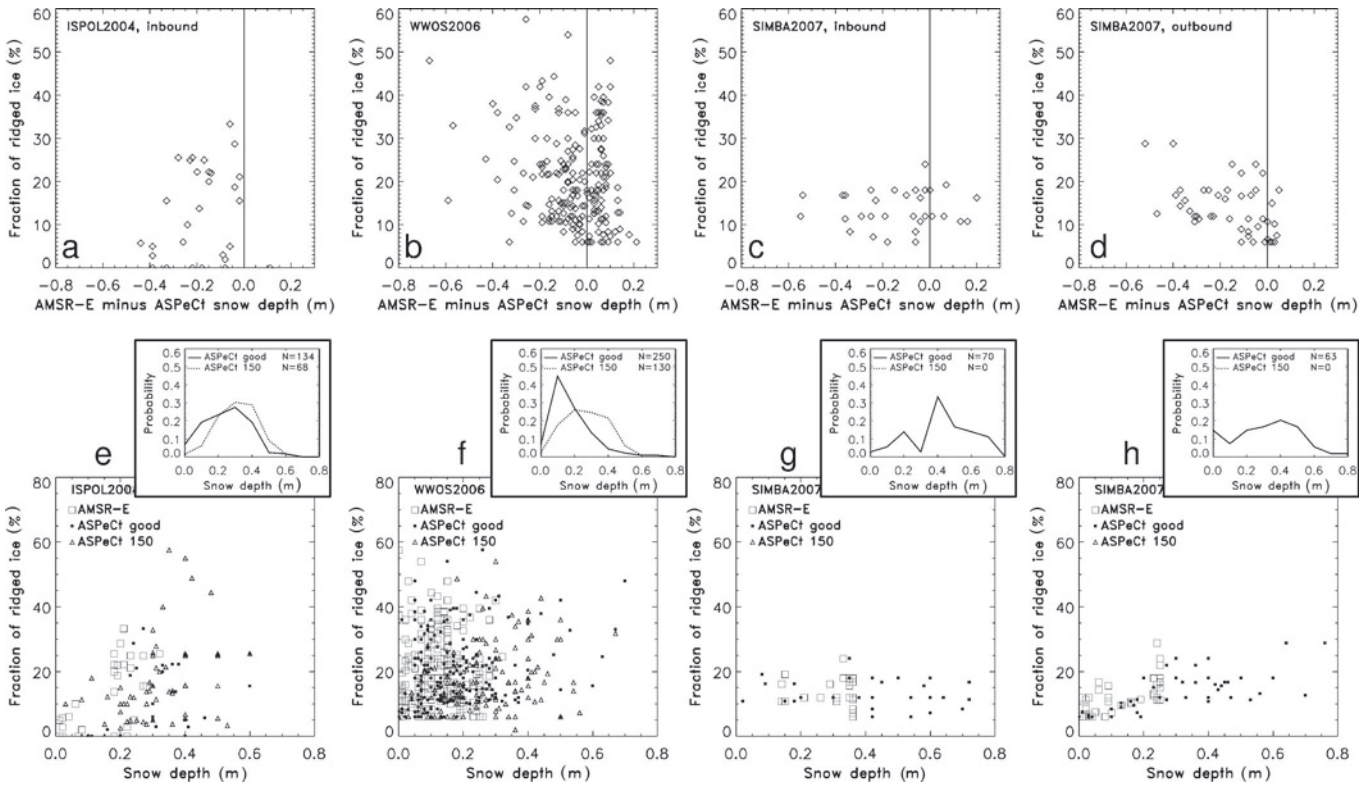

Fig. 4. (a–d) Fraction of ridged ice vs difference AMSR-E minus ASPeCt snow depth for ISPOL, WWOS and SIMBA in- and outbound cruise legs. (e–h) Fraction of ridged ice vs AMSR-E and ASPeCt snow depth values (open and filled squares), and ASPeCt snow depth values which coincide with an AMSR-E snow depth flagged as 150. The inset histograms give the probability distribution of the ASPeCt snow depths shown in the scatter plot below binned to 10 cm intervals; first interval is 0–5 cm, second 5–15 cm.

For ISPOL (Fig. 3a), AMSR-E snow depths agree to within 0.2 m with the ASPeCt snow depth; however, there seems to be a negative bias in the AMSR-E versus ASPeCt snow depth. Gaps in the shown valid (i.e. not flagged as 150) AMSR-E snow depth data can be seen for 24 and 26/27 November. During these days, ASPeCt ice type observations indicate MY ice. There seems to be no indication of an increased snow-depth difference with increased fraction of ridged ice from this image. For WWOS (Fig. 3b), the agreement between AMSR-E and ASPeCt snow depth seems to be better; in particular, there is no systematic negative bias. Again, on and around days when ASPeCt ice type observations indicate MY ice, no AMSR-E snow depth values are shown in Figure 3b, i.e. are flagged as 150. The fraction of ridged ice varied along the cruise track from 10% around 24 September to 20–40% in the period 28 September–5 October. For SIMBA in- and outbound legs (Fig. 3c and d), the agreement between ASPeCt and AMSR-E snow depth is relatively poor, particularly on 26 September and during 25/26 October when ASPeCt snow depths exceed AMSR-E snow depths by >0.2 m. This time, AMSR-E snow depths are not flagged as 150 whereas ASPeCt observations indicate the presence of MY ice. Fractions of ridged ice vary between 5% and 20% for the inbound, and between 5% and 28% for the outbound leg. However, their distribution along the cruise track does not seem to be related to the snow depth difference.

Figure 3e shows one example of coincident (to the observations given in Fig. 3d) σ^0_{KuHH} (diamonds) and the Ku-band VV- to HH-polarization radar backscatter ratio (σ^0_{KuVV} (dB) minus σ^0_{KuHH} (dB)) (triangles). This image reveals that σ^0_{KuHH} and the VV-/HH-polarization ratio remains relatively constant along the cruise track. In particular, there seems to be no relation with the snow depth differences observed on 25/26 October. Similar images have been produced from ISPOL and WWOS datasets but are not shown here since they do not give additional information.

Figure 4 sheds more light on a potential relationship between the fraction of ridged ice obtained from ASPeCt observations and the differences between AMSR-E and ASPeCt snow depth values. For ISPOL (Fig. 4a), AMSR-E snow depths tend to be biased by ~0.2 m towards lower values. For WWOS (Fig. 4b), differences are mostly between 0.1 and –0.2 m. A number of larger differences occur but are associated with both small and large fractions of ridged ice. For SIMBA inbound (Fig. 4c), there is no relationship between the fraction of ridged ice and the snow depth difference. For SIMBA outbound only (Fig. 4d), particularly large differences between ASPeCt and AMSR-E snow depths tend to be associated with higher fractions of ridged ice.

For ISPOL (Fig. 4e), valid (i.e. not flagged as 150) AMSR-E snow depths (grey squares) tend to increase with the ridged-ice fraction. This is not obviously the case for the coincident ASPeCt snow depths (black squares). However, ASPeCt snow depths that coincide with AMSR-E gridcells flagged as 150 ('invalid AMSR-E snow depth', henceforth (triangles)) also tend to increase with the ridged-ice fraction. For WWOS (Fig 4f), valid AMSR-E snow depths do not show the same trend as ISPOL showed. In this case, all snow depths (0–0.3 m) are associated with all fractions of ridged ice (5% to ~40%). The same can be said for the coincident ASPeCt snow depths. Again, ASPeCt snow depths coinciding with invalid AMSR-E snow depths tend to increase with the ridged-ice fraction. For SIMBA inbound (Fig. 4g), valid AMSR-E and ASPeCt

Table 1. Summary of σ^0 values obtained at the location of appropriate ASPeCt ship observations for all three cruises. Given are, from left to right, day of interest, time difference between ASPeCt observation and ASAR image acquisition, mean (averaged for the closest co-located 12.5 km x 12.5 km gridcell of the AMSR-E snow depth grid) radar backscatter values for Ku- and C-band (σ^0_{Ku} and σ^0_C) together with standard deviation (SD) for HH-polarization, local incidence angle in the ASAR image, total ice concentration IC, dominant ice type (MY = multi-year ice, PC = pancake ice, TFY, FY and THFY = thin, medium thick, and thick first-year ice), and ASPeCt and AMSR-E snow depth

Date	Δt	σ^0_{Ku}		σ^0_C			α	IC	Type	Snow depth	
		HH	S.D.	VV	HH	SD				ASPeCt	AMSR-E
[yyyymmdd]	min	dB	dB	dB	dB	dB	°	%		m	m
SIMBA											
20071024	3	–11.9	1.0	–14.3	–10.9	1.1	23	100	MY	0.30	0.25
20071025-I	3	–12.0	1.3	–14.0	–13.1	0.7	38	100	FY	0.70	0.23
20071025-II	29	–12.2	1.3	–14.5	–12.6	0.6	38	90	TFY	0.15	0.16
20071026	86	–12.6	1.4	–14.4	–11.8	0.6	32	100	TFY	0.45	0.06
20071027	5	–12.1	1.5	–13.5	–9.5	0.7	24	80	PC	0.08	OW
ISPOL											
20041117	58	–8.2	1.5	–12.3	–13.0	1.0	32	80	FY	0.25	–
20041121	57	–10.7	1.4	–12.9	–14.0	1.3	36	80	FY	0.15	–
20041125	74	–13.1	1.3	–15.7	–15.7	0.9	41	80	THFY	1.00	0.30

snow depths do not show a relationship with the ridged-ice fraction. For SIMBA outbound (Fig. 4h), valid AMSR-E and ASPeCt snow depths increase with the ridged-ice fraction.

The two modal values of the ASPeCt snow depth distributions derived for ISPOL (histogram, Fig. 4e) are almost similar and indicate only slightly higher values for invalid AMSR-E snow depths. For WWOS, however, (histogram, Fig. 4f) the two modal values differ on average by 0.1 m: ASPeCt snow depths coinciding with invalid AMSR-E snow depths are larger than those coinciding with valid AMSR-E snow depths. The histogram based on the valid AMSR-E snow depths is skewed towards small snow depth values, while the histogram based on the invalid AMSR-E snow depths has an almost normal distribution. This suggests that at least in this case, a large portion of gridcells that would potentially contain relatively high snow depth values is flagged invalid in the AMSR-E snow depth product. Accordingly, an average snow depth calculated from the AMSR-E snow depth product might be biased low.

4.2. Snow depth versus radar backscatter

Table 1 shows ASPeCt and coincident AMSR-E snow depths together with coincident C- and Ku-band radar backscatter values. This table does not allow any conclusion about a relationship between snow depth and radar backscatter values. For SIMBA, variations in σ^0_{CHH} and σ^0_{KuHH} between different ship positions are small, and for σ^0_{CHH} are mostly explained by local incidence angle variations (Ozsoy-Cicek and others, in press). For ISPOL, variations are larger, particularly for σ^0_{KuHH}, but the lack of coincident triplets of ASPeCt snow-depth, σ^0_{CHH} and σ^0_{KuHH} data hampers any further interpretation. Note that the time series of σ^0_{KuHH} shown together with the snow depth time series in Figure 3 does not indicate the anticipated systematic change that we intended to relate to those ASPeCt snow depth observations where AMSR-E snow depths are biased.

The discrepancies in snow depth between ASPeCt and AMSR-E shown in Table 1 (20071025-I and 20071026 as well as 20041125) should also not to be over-interpreted, as the variability in the ASPeCt snow depths is of course much higher than that of the AMSR-E snow depths (see Figs 2 and 3). The snow depth of 1.0 m observed during ISPOL on 25 November (Table 1: 20041125) is a singular event in a series of much smaller snow depths of ~0.4 m which agree within 0.15 m with AMSR-E snow depths (Fig. 3a). In contrast, snow depths of 0.70 and 0.45 m observed during SIMBA on 25 and 26 October (Table 1: 20071025-I and 20071026) seem to belong to an area where ASPeCt snow depths are continuously larger than the AMSR-E snow depth (Fig. 3d). This is also supported by Figure 2c and d: some of the average ASPeCt snow depths stand out clearly against the smaller AMSR-E snow depths in the background.

Figure 5a–c show an example of the remote-sensing datasets, on which the further analysis is based (see last paragraph of section 3): an ASAR image, a QuikSCAT σ^0_{KuHH} image and an AMSR-E snow depth map. The white rectangular frames in Figure 5b and c denote the region covered by the ASAR image. Note the difference in the location of the ice edge in Figure 5b compared to Figure 5a and c; this is caused by the fact that during this time the ice edge was advancing rapidly northwards. This process cannot be resolved with the 5 day (8–12 October) average AMSR-E snow depth shown in Figure 5b.

The unimodal histogram shown in Figure 5d reveals modal σ^0_{Ku} values of –15.5 and –13.6 dB for VV- and HH-polarization, respectively, and a modal σ^0_{CHH} value of –12.0 dB (see Ozsoy-Cicek and others, in press). The histograms given in Figure 5e reveal that Ku-band VV-/HH-polarization ratio values tend to be normally distributed across the ice-covered part of the image (modal value –2.3 dB). The σ^0_{KuHH} standard deviation is also normally distributed, while the σ^0_{CHH} standard deviation has a skewed distribution with almost three modes: 1.0 and 2.0 dB (and 0.6 dB). This distribution is caused by the presence of different ice types: fast ice, drift ice and the marginal ice zone (MIZ) which stands out clearly in Figure 5a at ~68° S. Averaging the 125 m grid resolution ASAR image over 12.5 km in a region with radar backscatter values that vary by 10 dB over the scale of ~1 km, as in the MIZ, causes the mentioned mode of high standard deviations in Figure 5e. The areal extent of the fast ice cover in our region of interest is rather small. From visual inspection of the full SIMBA dataset

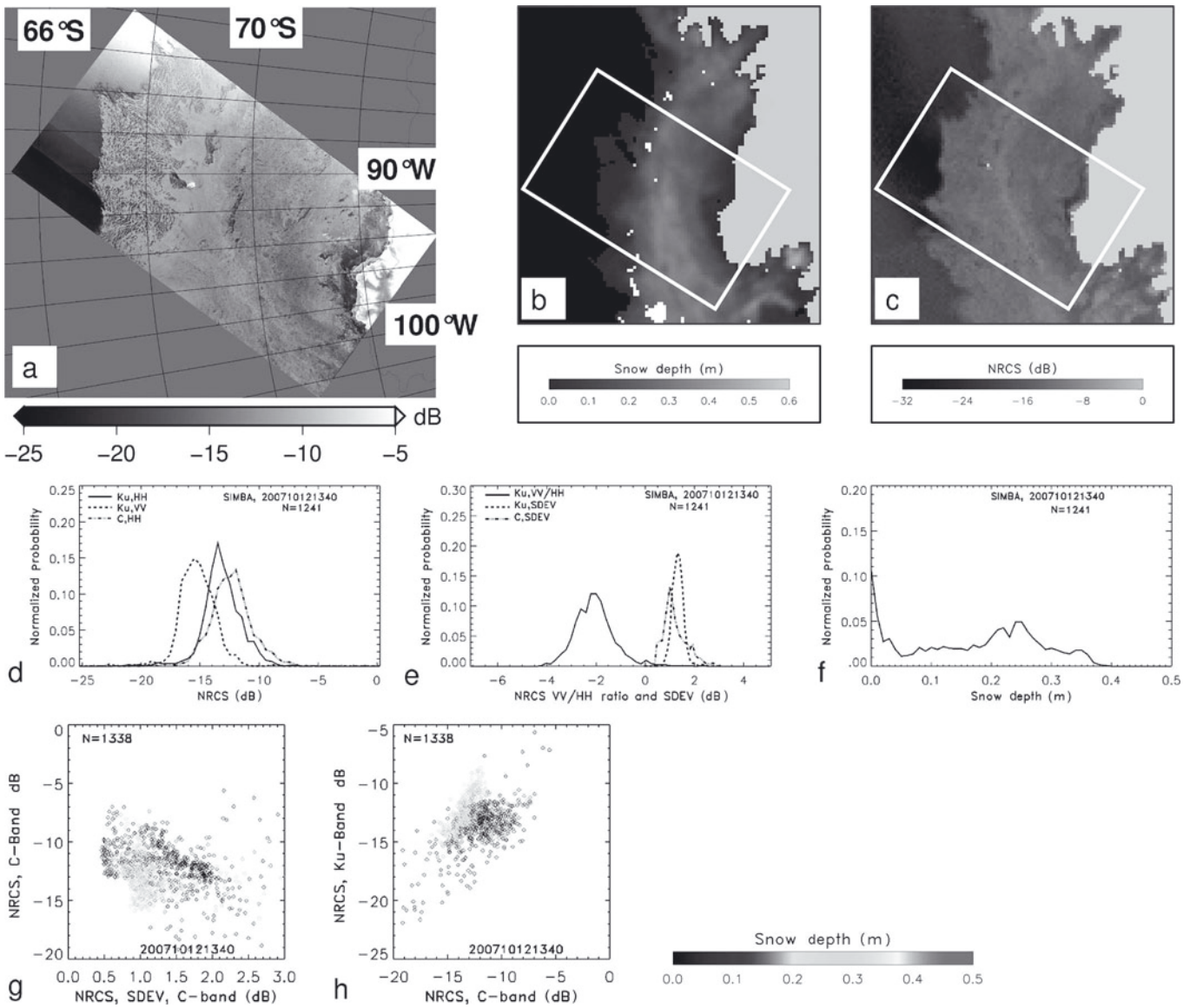

Fig. 5. Example of involved datasets for 12 October 2007 SIMBA cruise. (a) ASAR WSM σ^0_{CHH} image acquired at 13:40 UTC; grid resolution 125 m; legend below the image. (b) AMSR-E snow depth at 12.5 km grid resolution; white, grey and black areas denote regions flagged as 150, land and open water, respectively; (c) QuikSCAT σ^0_{KuHH} image at 12.5 km grid resolution; land is flagged grey. White rectangles in (b) and (c) mark the area covered by the SAR image shown in (a). (d) Histograms of σ^0_{CHH}, σ^0_{KuVV} and σ^0_{KuHH} obtained at 12.5 km grid resolution within (a) and the white rectangle in (c). (e) Histograms of the Ku-band VV/HH polarization ratio together with histograms of the σ^0 standard deviation of same area as in (d). (f) Histogram of AMSR-E snow depth values within the rectangle in (b). (g) σ^0_{CHH} at 12.5 km grid resolution vs its standard deviation. (h) σ^0_{KuHH} vs σ^0_{CHH}. Values shown in (g) and (h) are scaled with the coincident AMSR-E snow depth within the respective gridcell. The number *N* (d–h) denotes the number of used ice-covered gridcells with at least 60% ice concentration.

σ^0_{CHH} standard deviation maps (not shown), we know that the majority of the observed low standard deviations originate from a narrow zone of a very uniform radar backscatter signature. This zone is found between the MIZ and drift ice closer to the coast (see Fig. 5d, close to, east and west of Peter I Island situated at 69° S, 90.5° W). This zone most likely comprises first-year ice with floe sizes ~50–100 m and a quite substantial snow cover of up to 0.45 m (Table 1: 20071026; Ozsoy-Cicek and others, in press).

Figure 5f shows the snow depth distribution; it has two modes. One is situated at ~0 cm which is the new ice forming in the MIZ, and in the polynyas adjacent to the coast (Fig. 5a). This mode is absent until about 9 October but afterwards shows the highest or at least the second highest probability because of the increasing new ice fraction due to the ice edge advance. The second mode, situated at ~0.2 m, is present during the entire SIMBA period, and decreases towards the end of October. Finally, there is evidence for a third mode comprising higher snow depths (0.35 m).

Figure 5g and h display the aforementioned scatter plots (see last paragraph of section 3), and reveal some clustering of σ^0_{CHH} (mean and standard deviation) values with AMSR-E snow depth values (Fig. 5g), as does the combination of σ^0_{KuHH} and σ^0_{CHH} (Fig. 5h). We revisit these two combinations later.

In Figure 6 we look at the general development of the mean AMSR-E snow depth (Fig. 6a and d) in comparison to the mean values of σ^0_{KuHH}, σ^0_{KuVV} and σ^0_{CHH} (Fig. 6b and e) for the SIMBA period. Mean snow depths in regions PETERIA_ASC and PETERIA_DES decrease from an initial value of 0.20 m at the beginning of October to about 0.09 m on 10 November 2007. Time series derived for the other two

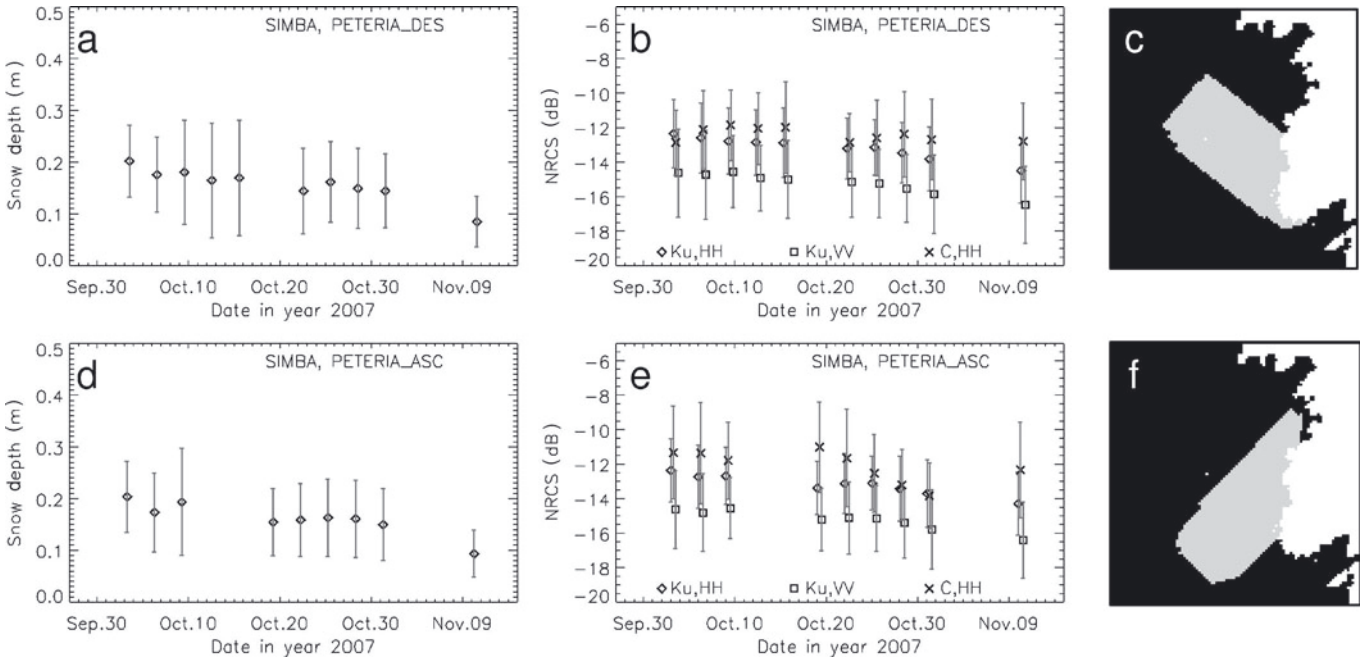

Fig. 6. Time series of the ASAR image area-averaged (only gridcells inside the ASAR image overlap masks, >60% ice concentration and situated north of 73° S) snow depth (a, d), and σ^0_{CHH}, σ^0_{KuVV} and σ^0_{KuHH} (b, e) for all available 3 day repeat-pass Envisat ASAR images of the regions PETERIA_DES (a, b) and PETERIA_ASC (d, e), locations of which are given in (c) and (f). Vertical bars denote one standard deviation. Gaps in the time series are caused by (1) ASAR images that were not acquired within the selected time slot of ±15 min (see section 3) or (2) ASAR images that cover too small a portion of the ASAR image overlap mask.

ASAR image groups (not shown) are shorter but also reveal this decreasing trend.

Mean σ^0_{Ku} tends to decrease by 1–2 dB (Fig. 6b and e). This gradual decrease could be caused by increased attenuation of microwave radiation in an, on average, increasingly wet snow cover. The increasing solar radiation at this time of year could be one driver for elevated snow wetness due to internal snowmelt, provided that clear-sky conditions prevail. Modelled air temperatures (Table 2) reveal that after a cold 5 day period (pentad) (26–30 October), air temperatures increased at the latitude of Peter I Island until the last pentad shown (4–9 November). On 10 November, air temperatures were between –1.5°C and –3°C, high enough to observe liquid water in snow on sea ice (e.g. Garrity, 1992). The Ku-band VV-/HH-polarization ratio stayed constant at ~2 dB.

The mean σ^0_{CHH} is almost constant and stays within the variability given by the error bars (one standard deviation) for region PETERIA_DES (Fig. 6b) but is more variable over time in the other region (Fig. 6e). The observed decrease in σ^0_{CHH} by 3 dB over a period of 12 days (Fig. 6e), and other variations in σ^0_{CHH} that are not further discussed here, can be assigned to changes in the mean σ^0_{CHH} distribution caused by the change from a compact to an open, divergent sea-ice cover. These changes can be identified in the SIMBA 2007 Envisat ASAR image dataset by interpreting the distributions of σ^0_{CHH} and its standard deviation. While a compact ice cover does not contain any leads and exhibits a compact ice edge, the open ice cover can contain lots of leads, a divergent ice edge and is additionally associated with polynya formation along the coast. Figure 5a shows an example of an open ice cover with the characteristic signature of dark and bright bands in the MIZ which indicate areas of new ice (low σ^0_{CHH}) and pancake ice (high σ^0_{CHH}), with a number of leads covered by new ice in the pack ice, and a polynya at the coast, also covered by new ice. The observed changes in the ice conditions and thus in σ^0_{CHH} can be related to changes in the mean wind direction, as can be deduced from Table 2 showing the meridional component of the modelled mean 5 day wind speed.

Table 2. Mean 1000 hPa level air temperature and *v*-component of the wind speed at 69° S and the given longitude as derived online using data of the operational US National Centers for Environmental Prediction (NCEP)/US National Center for Atmospheric Research (NCAR) weather forecasting model (http://www.esrl.noaa.gov/psd/data/histdata). Positive (negative) values of *v* denote a southerly (northerly) wind component

Long.	Variable	1–5 Oct.	6–10 Oct.	11–15 Oct.	16–20 Oct.	21–25 Oct.	26–30 Oct.	31 Oct.–4 Nov.	5–9 Nov.
80° W	*T* (°C)	–0.5	–3.5	–10.0	–7.0	–1.5	–6.0	–6.0	–4.0
	v (m s^{-1})	–4.0	+1.0	+4.0	–3.0	–4.0	+5.0	+2.0	+4.0
90° W	*T* (°C)	–2.0	–4.0	–10.0	–6.0	–3.5	–11.5	–7.0	–5.0
	v (m s^{-1})	–1.0	0.0	+2.5	–4.0	–1.5	+4.5	+1.0	+3.0
100° W	*T* (°C)	–5.5	–5.5	–9.0	–4.0	–5.0	–10.0	–6.0	–3.0
	v (m s^{-1})	+1.0	–1.5	+1.5	–4.0	+3.0	+4.5	0.0	–1.0

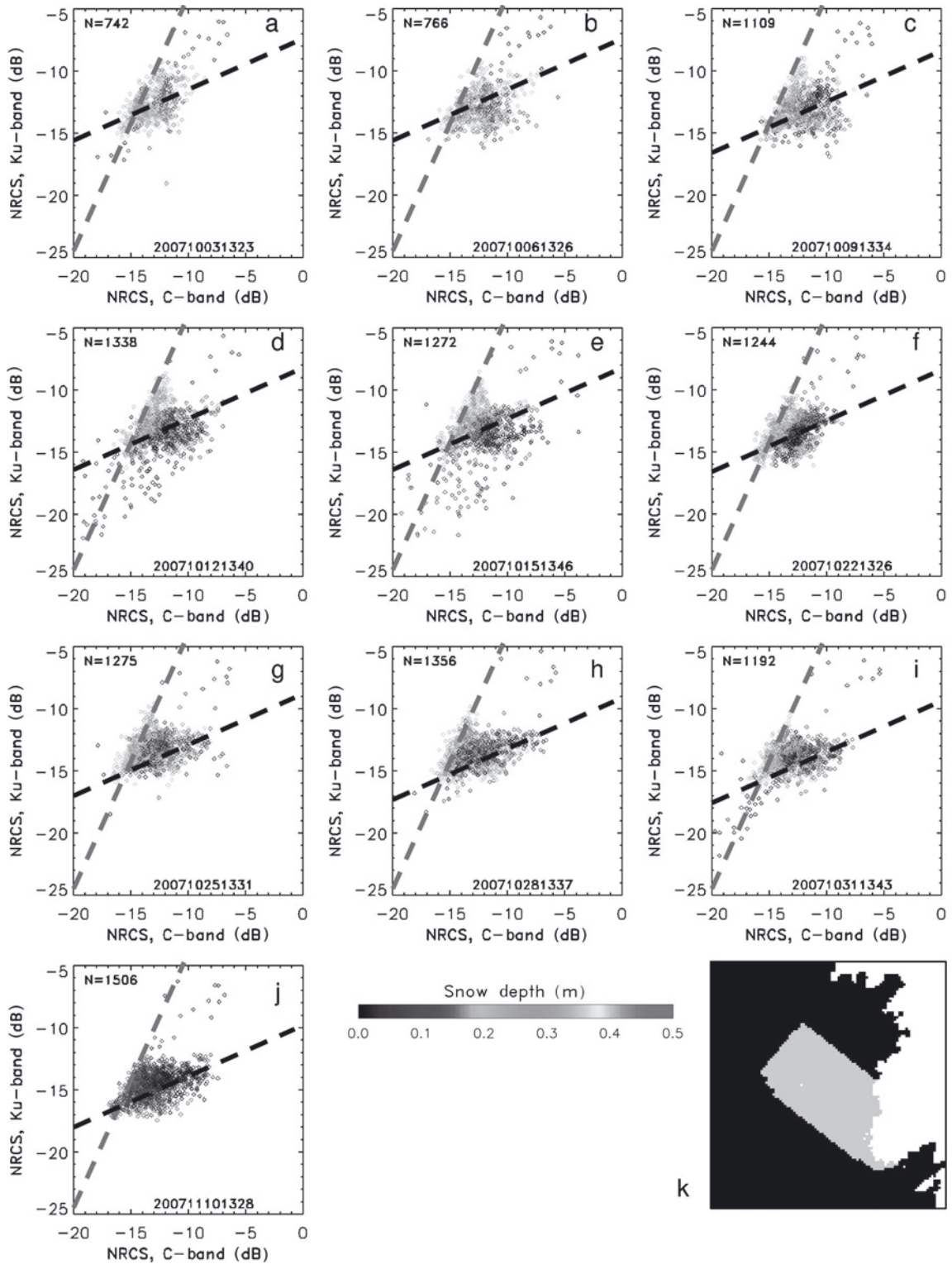

Fig. 7. Scatter plots of σ^0_{KuHH} vs σ^0_{CHH} for all 3 day repeat pass ASAR for region PETERIA_DES (see also Fig. 6a and b) between 3 October and 10 November 2007. All symbols are colour-coded according to the AMSR-E snow depth within the respective co-located gridcell. The map given in (k) denotes the location of region PETER1A_DES. Dashed red and black lines are shown to indicate a preferential alignment of data points along two 'clouds', which are referred to as STC and SHC in the text.

We chose region PETERIA_DES (Fig. 6c) for further investigation because it contains the largest number of different ice types – fast ice, polynya, pack ice and MIZ – and was investigated in the case study by Ozsoy-Cicek and others (in press). Figure 7 shows σ^0_{KuHH} versus σ^0_{CHH} scaled with AMSR-E snow depths (see Fig. 5g). The plots in Figure 7 reveal an elongated 'cloud' of σ^0_{KuHH}–σ^0_{CHH} pairs with snow depths above ~0.2 m, which stretches along the red dashed line and can be tracked through almost all plots. There is evidence for a second elongated 'cloud' of

σ^0_{KuHH}– σ^0_{CHH} pairs with snow depths at or below 0.2 m. This stretches along the dashed black line and can also be tracked through almost all plots. In contrast to the aforementioned 'cloud' (red dashed line), this one is not very well defined, particularly in Figure 7a–c, and it shifts over time by 2–3 dB towards lower σ^0_{KuHH} values (cf. Fig. 7b).

The 'cloud' with the steeper slope (steeply sloping cloud (STC)) covers a larger (smaller) range of σ^0_{KuHH} (σ^0_{CHH}) values, while the 'cloud' with the shallower slope (shallowly sloping cloud (SHC)) covers a smaller (larger) range of σ^0_{KuHH} (σ^0_{CHH}) values. The SHC extends into that σ^0_{CHH} range, which seems to be typical for the zone of rough cake-ice-like first-year ice south of the MIZ (Table 1: 20071026; Fig. 5a). We suggest that, with this 'cloud', rough first-year ice regions could be identified.

According to a case study carried out with data from 12 October 2007 (Ozsoy-Cicek and others, in press), σ^0_{KuHH} and σ^0_{KuVV} occupy a rather narrow range (~2 dB) regardless of the ice type, while σ^0_{CHH} values occupy a wide range in the perennial ice region and in the MIZ. Our new results differ from these earlier findings, in that the range of σ^0_{KuHH}, especially in the STC (red dashed line, Fig. 7), is much larger (at least 5 dB). This is possibly due to a difference in selecting the data. In this study, we did not look at areas that, in accordance with coincident C-band SAR imagery, belong to specific ice types (Ozsoy-Cicek and others, in press) but rather examined the entire ice-covered area within the co-located ASAR image (Fig. 3a and c). The STC tends to be associated with, on average, larger snow depths than the SHC (see above), and average σ^0_{CHH} values are relatively low, i.e. about –14 dB. We suggest therefore that the STC may be associated with merely undeformed first- or second-year ice, the snow cover of which is subject to the onset of melt–refreeze cycles which can cause σ^0_{KuHH} to vary while σ^0_{CHH} remains stable.

The STC is relatively well defined but the SHC is not. Here actually two clouds do overlap, at least temporarily. One is caused by the expansion of the MIZ, starting after 6 October, and the other is the one that is visible before this expansion (Fig. 7b and c). We prepared a series of plots similar to that shown in Figure 7 for σ^0_{CHH} vs its standard deviation (not shown). We found that thin snow (<0.2 m) seems to be associated with high σ^0_{CHH} (~–12 dB), while thick snow (>0.2 m) seems to coincide with low σ^0_{CHH} (~–14 dB). However, at the same time, standard deviations are low, i.e. <0.8 dB, as would be typical for the zone of rough first-year ice discussed in the context of Figure 5e. As time progresses, the amount of data pairs with low σ^0_{CHH} standard deviations, high σ^0_{CHH} and snow depths below 0.15 m increases. According to the observations during the SIMBA outbound leg, this zone of rough first-year ice is potentially one of the regions where AMSR-E snow depths underestimate ASPeCt snow depths (Table 1). We found further that low AMSR-E snow depths, i.e. <0.05 m, are associated with the MIZ, particularly during ice-edge advance, as is evident from predominant high σ^0_{CHH} standard deviations (1.1–2.5 dB). By means of these findings we can distinguish two subsets of σ^0KuHH–σ^0_{CHH} data pairs in the SHC. One exhibits a small σ^0_{CHH} standard deviation of <0.8 dB, and is thus associated with the aforementioned zone of rough first-year ice. The second exhibits high σ^0_{CHH} standard deviation (>1.5 dB), and is thus associated with the MIZ.

5. CONCLUSIONS

We compared ship-based observations carried out according to the ASPeCt protocol with co-located AMSR-E snow depth values for two cruises in the Weddell Sea (ISPOL, November 2004; WWOS, September/October 2006) and for one cruise in the Bellingshausen Sea (SIMBA, September/October 2007). Most (>75%) of the snow depths agree within a range of 0.2 m for the considered WWOS and SIMBA observations. However, AMSR-E snow depths can underestimate ASPeCt snow depths by 0.2–0.4 m for rough ice regions, particularly for SIMBA, or in other words by a factor between 2 and 4 (comparable with Worby and others, 2008). AMSR-E snow depths are correctly flagged as 150 where multi-year ice was observed during ISPOL and WWOS cruises. In contrast, AMSR-E snow depth was not flagged as 150 where SIMBA ASPeCt observations indicate multi-year ice. AMSR-E snow depths flagged as 150 coincide with larger ASPeCt snow depths than valid (i.e. not flagged) AMSR-E snow depths for ISPOL and WWOS. For WWOS, and more clearly for SIMBA outbound, the difference between AMSR-E and ASPeCt snow depths increases as the fraction of ridged ice increases.

Neither Envisat ASAR C- nor SeaWinds QuikSCAT Ku-band satellite radar backscatter data allow us to identify regions that exhibit a large difference in snow depth between ASPeCt and satellite data for the considered cruise tracks, mainly because we have too few coincident data. The observed decrease in ASAR-image ice-area averaged σ^0_{KuHH} and σ^0_{KuVV} values (by ~2 dB) is likely to be associated with an increase in the snow liquid-water content in accordance with an increase in modelled near-surface air temperatures to values above –5°C during SIMBA. Also for SIMBA, the weekly to biweekly variation in average σ^0_{CHH} by up to 3 dB is related to changes between divergent and convergent ice conditions in accordance with the modelled meridional surface wind-speed component. Apart from this variation, σ^0_{CHH} remains constant within one standard deviation. The ASAR-image ice-area averaged AMSR-E snow depth decreased from ~0.2 m to ~0.1 m during October 2007.

We identified two data-pair 'clouds' which each align along a line with a different slope in scatter plots of σ^0_{KuHH} vs σ^0_{CHH} scaled with the AMSR-E snow depth. We suggest that the more steeply sloping cloud could be used to identify different stages of snow metamorphism on undeformed first- or second-year ice because snow depths are high (>0.2 m), σ^0_{CHH} values relatively low and stable, and σ^0_{KuHH} values variable. The cloud with the shallow slope could be used to identify those rough-ice regions where AMSR-E snow depths tend to underestimate the actual snow depth, because snow depths are low (<0.15 m) and σ^0_{CHH} values span a wide range and particularly comprise high values. In this second cloud, σ^0_{CHH} standard deviations could in addition permit differentiation between the MIZ (high standard deviation; AMSR-E snow depths agree with ASPeCt snow depths) and the zone of rough first-year ice situated south of the MIZ (low σ^0_{CHH} standard deviation; AMSR-E snow depths likely to be too small).

Work is planned to carry out a cluster analysis in three-dimensional space involving σ^0_{CHH}, its standard deviation and σ^0_{KuHH} based on the SIMBA dataset. The results of this cluster analysis could be applied to co-located and coincident σ^0_{CHH} and σ^0_{KuHH} maps in order to obtain an estimate of the spatio-temporal distribution of the aforementioned sea-ice types and potential snow-property

changes. This information might further improve our understanding of relationships between satellite observations of the radar backscatter of Antarctic sea ice and related snow and sea-ice property changes. The information so obtained might further be used to delineate regions where AMSR-E snow depths are biased because of the influence of melt–refreeze cycles or rough sea ice on the AMSR-E brightness temperatures used in the current snow-depth algorithm. A further assessment of the influence of the different Envisat ASAR surface incidence angles, of the influence of the different ice types on the spatial variability of σ^0 on scales of 1–10 km, and of the validity of the ASPeCt observations would also be an important step in this direction.

ACKNOWLEDGEMENTS

This work was supported by the German Science Foundation (DFG): SFB 512-TP E5. We acknowledge US National Science Foundation (NSF) grant ANT AWT0703682 and NASA grant NNX08AQ87G to the University of Texas at San Antonio (UTSA) for support. We acknowledge AMSR-E data provision by the NSIDC in Boulder, CO, USA. The European Space Agency (ESA) and P. Heil (principal investigator for ESA) are thanked for providing Envisat ASAR images (© ESA 2007). Additional Envisat images provided by ESA through Category-1 project (ID No. 6097) to UTSA are greatly appreciated. We are also grateful to sea-ice observers aboard R/V *Nathaniel B. Palmer* and *Polarstern* as well as the entire crew and science team during ISPOL, WWOS and SIMBA. The Python code for processing and calibration of the Envisat ASAR images was kindly provided by L. Kaleschke. The helpful comments of two anonymous reviewers as well as the scientific editor, R. Massom, significantly improved the manuscript. Enhanced-resolution QuikSCAT data were acquired from the BYU Center for Remote Sensing. The International Space Science Institute, Bern, Switzerland, is acknowledged for supporting this study via projects 184, 137 and 169.

REFERENCES

Attema, E. *and 10 others*. 1998. ASAR science and applications. *ESA Rep.* SP-1225.

Comiso, J.C., D.J. Cavalieri and T. Markus. 2003. Sea ice concentration, ice temperature, and snow depth using AMSR-E data. *IEEE Trans. Geosci. Remote Sens.,* **41**(2), 243–252.

Early, D.S. and D.G. Long. 2001. Image reconstruction and enhanced resolution imaging from irregular samples. *IEEE Trans. Geosci. Remote Sens.,* **39**(2), 291–302.

Fichefet, T. and M.A. Morales Maqueda. 1999. Modelling the influence of snow accumulation and snow-ice formation on the seasonal cycle of the Antarctic sea-ice cover. *Climate Dyn.,* **15**(4), 251–268.

Garrity, K. 1992. Characterization of snow on floating ice and case studies of brightness temperature change during the onset of melt. *In* Carsey, F.D. *and 7 others, eds. Microwave remote sensing of sea ice*. Washington, DC, American Geophysical Union, 313–328. (Geophysical Monograph Series 68.)

Haas, C. 2001. The seasonal cycle of ERS scatterometer signatures over perennial Antarctic sea ice and associated surface ice properties and processes. *Ann. Glaciol.,* **33**, 69–73.

Haas, C., A. Friedrich, Z. Li, M. Nicolaus, A. Pfaffling and T. Toyota. 2009. Regional variability of sea ice properties and thickness in the northwestern Weddell Sea obtained by in-situ and satellite measurements. *In* Lemke, P., *ed. The expedition ANTARCTIC XXIII/7 of the Research Vessel 'Polarstern' in 2006*. Bremerhaven, Alfred Wegener Institute for Polar and Marine Research. (Reports on Polar and Marine Research 586.)

Hellmer, H.H., M. Schröder, C. Haas, G.S. Dieckmann and M. Spindler. 2008. The ISPOL drift experiment. *Deep-Sea Res. II,* **55**(8–9), 913–917.

Huang, S. and F. Siegert. 2004. ENVISAT multisensor data for fire monitoring and impact assessment. *Int. J. Remote Sens.,* **25**(20), 4411–4416.

Kwok, R., G.F. Cunningham, H.J. Zwally and D. Yi. 2006. ICESat over Arctic sea ice: interpretation of altimetric and reflectivity profiles. *J. Geophys. Res.,* **111**(C6), C06006. (10.1029/2005JC003175.)

Lewis, M.J. *and 6 others*. In press. Sea ice and snow cover characteristics during the winter–spring transition in the Bellingshausen Sea: an overview of SIMBA 2007. *Deep-Sea Res. II*. (10.1016/j.dsr2.2010.10.027.)

Maksym, T. and T. Markus. 2008. Antarctic sea ice thickness and snow-to-ice conversion from atmospheric reanalysis and passive microwave snow depth. *J. Geophys. Res.,* **113**(C2), C02S12. (10.1029/2006JC004085.)

Markus, T. and D.J. Cavalieri. 1998. Snow depth distribution over sea ice in the Southern Ocean from satellite passive microwave data. *In* Jeffries, M.O., *ed. Antarctic sea ice: physical processes, interactions and variability*. Washington, DC, American Geophysical Union, 19–39. (Antarctic Research Series 74.)

Markus, T. *and 8 others*. 2006a. Microwave signatures of snow on sea ice: observations. *IEEE Trans. Geosci. Remote Sens.,* **44**(11), 3081–3090.

Markus, T., D.C. Powell and J.R. Wang. 2006b. Sensitivity of passive microwave snow depth retrievals to weather effects and snow evolution. *IEEE Trans. Geosci. Remote Sens.,* **44**(1), 68–77.

Massom, R.A. *and 12 others*. 2001. Snow on Antarctic sea ice. *Rev. Geophys.,* **39**(3), 413–445.

Ozsoy-Cicek, B., S. Kern, S.F. Ackley, H. Xie and A.E. Tekeli. In press. Intercomparisons of Antarctic sea ice types from visual ship, RADARSAT-1 SAR, Envisat ASAR, QuikSCAT, and AMSR-E satellite observations in the Bellingshausen Sea. *Deep-Sea Res. II*. (10.1016/j.dsr2.2010.10.031.)

Stroeve, J.C. *and 8 others*. 2006. Impact of surface roughness on AMSR-E sea ice products. *IEEE Trans. Geosci. Remote Sens.,* **44**(11), 3103–3117.

Willmes, S., J. Bareiss, C. Haas and M. Nicolaus. 2006. The importance of diurnal processes for the seasonal cycle of sea-ice microwave brightness temperatures during early summer in the Weddell Sea, Antarctica. *Ann. Glaciol.,* **44**, 297–302.

Willmes, S., C. Haas and M. Nicolaus. In press. High radar-backscatter regions on Antarctic sea ice and their relation to sea-ice and snow properties and meteorological conditions. *Int. J. Remote Sens.* (10.1080/01431161003801344.)

Wingham, D.J. *and 15 others*. 2006. CryoSat: a mission to determine the fluctuations in Earth's land and marine ice fields. *Adv. Space Res.,* **37**(4), 841–871.

Worby, A.P., I. Allison and V. Dirita. 1999. A technique for making ship-based observations of Antarctic sea ice thickness and characteristics. Part I. Observational techniques and results. *Antarct. CRC Res. Rep.* 14.

Worby, A.P., T. Markus, A.D. Steel, V.I. Lytle and R.A. Massom. 2008. Evaluation of AMSR-E snow depth product over East Antarctic sea ice using in situ measurements and aerial photography. *J. Geophys. Res.,* **113**(C5), C05S94. (10.1029/2007JC004181.)